

# Comparison of Three Interacting V-Flames to a Single Bluff Body Flame at Two Reynolds Numbers

Wyatt Culler\*, Ankit Tyagi†

*The Pennsylvania State University, University Park, Pennsylvania, 16802*

Prabhakar Venkateswaran‡

*Trinity College, Hartford, Connecticut, 06106*

and

Jacqueline O'Connor§

*The Pennsylvania State University, University Park, Pennsylvania, 16802*

The axial velocity profiles for three interacting bluff-body flames at Reynolds numbers of 4000 and 6000 are compared to a single-flame case at the same Reynolds numbers and equivalence ratio of  $\phi=0.8$ . To facilitate a direct comparison between interacting and single-flame behaviors, an interacting flame case has been chosen to have a very similar time-averaged flow field as the single-flame configuration. While the inlet turbulence levels of the single-flame and interacting flame configurations are the same, the turbulence field development is different when multiple flames are present, leading to higher reactant Reynolds stresses along the  $\bar{c} = 0.5$  contour in the cross-stream direction when there is flame interaction. The principal directions are calculated and show that the flame surface normals tend to align with most compressive principal strain. Flame surface density is quantified for both flame configurations and indicates there is more flame wrinkling when flame interaction is present. The higher cross-stream Reynolds stresses cause increased flame wrinkling which results in faster flame brush growth when there is flame interaction. Flames are found to anisotropically redistribute turbulent kinetic energy, preferentially enhancing cross-stream fluctuations in the products. These results demonstrate that the multiple bluff-body flame behavior cannot be considered a superposition of the dynamics of the single bluff-body flame.

## Nomenclature

$D$	=	bluff body size
$Y_{int}$	=	time averaged flame intersection point
$\bar{c}$	=	time-averaged progress variable
$u$	=	axial velocity
$u'$	=	magnitude of turbulent velocity fluctuations
$y$	=	cross-stream direction
$x$	=	streamwise direction
$\phi$	=	equivalence ratio
$RMS$	=	root-mean-square
$\bar{\Sigma}$	=	time averaged flame surface density
$S_{ij}$	=	strain rate tensor
$\theta_p$	=	principal angle
$\theta$	=	flame normal angle relative to reactants
$N$	=	number of frames
$L$	=	length of flame
$A$	=	area of circle
$FSD$	=	flame surface density

---

\* Mechanical and Nuclear Engineering, 15 Research East Building, University Park, PA, AIAA Student Member

† Mechanical and Nuclear Engineering, 15 Research East Building, University Park, PA, AIAA Student Member

‡ Department of Engineering, 300 Summit Street, Hartford, CT

§ Mechanical and Nuclear Engineering, 111 Research East Building, University Park, PA, AIAA Member

## I. Introduction

FLAME interaction is an important phenomenon that occurs in a number of combustion technologies including gas turbines for both power generation and aircraft propulsion. Previous studies have shown that flame interaction causes changes in both the global and local flame behavior [1-3]. The time-averaged flame shape, flame static stability, and flame dynamic stability can vary with different levels of flame interaction. In this study, flame interaction is investigated using three interacting, planar, V-flames stabilized on triangular bluff bodies. Flameholders such as these are used in duct burners and afterburners. We have chosen this configuration to investigate fundamental flame and flow interaction processes as the configuration is largely two-dimensional, allowing for the use of planar diagnostics. The goal of this work is to compare the structure and turbulent characteristics of both the flow field and flame in a single-flame and multiple-flame configuration.

The time-averaged flow field around and behind a bluff body includes three important regions, as shown in Figure 1: the boundary layer along the bluff body, the separated free shear layer, and the wake [4, 5]. The boundary layer forms at the leading edge of the bluff body and develops until the separation points at the edges of the bluff body. The shear layers that develop from the separation points form the outer boundary of the recirculation zone, and interact further downstream. In the absence of combustion, the wake is subject to both the von-Karman and shear layer instabilities [6]. Combustion suppresses the von-Karman instability [7], provided the density ratio across the flame is sufficiently high, making the shear layer instability the dominant instability. This instability manifests itself as a symmetric billowing of the flame due to the symmetric vortex rollup. In the reacting flow the wake also transitions to a jet farther downstream due to the gas expansion across the flame.

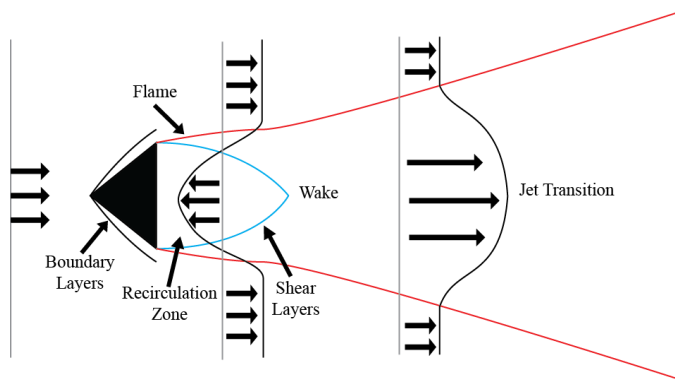


*Figure 1: Time averaged flow field for a single bluff body flame. Adapted from [4, 5].*

The bluff body wake flow is a high shear flow with an anisotropic turbulence field. Turbulent characteristics in the near-wake region of non-reacting bluff body flows have been measured by both hot-wires [8, 9] and particle image velocimetry (PIV) [10]. Ong and Wallace [9] report the Reynolds stress components at different downstream locations and show that both the streamwise and cross-stream Reynolds stresses decrease with increasing distance from the bluff body. They also show that the distribution of the cross-stream and streamwise Reynolds stresses is anisotropic, with cross-stream fluctuations being larger than streamwise fluctuations at a given downstream location. Similar trends are reported by Zhou and Antonia [8] and Braza *et al.* [10]. These turbulence profiles change in the presence of a flame, as numerous studies have shown that flame-flow coupling can significantly alter the turbulent characteristics of a flow field [11-16]. In the flamelet regime, the reactant gas turbulence causes the flame to wrinkle and is responsible for the development of a flame brush [17]. Whereas the flame location in a laminar flow may be stationary, the flame wrinkling and motion in a turbulent flow results in the need for a statistical description of the flame location, which is achieved through the concept of the flame brush. The flame brush quantifies the region in space where the flame can be found [17], and is larger in higher turbulence flows as a result of the more violent motion of the flame [18]. The flame brush thickness can be defined in multiple ways [19], and typically grows nonlinearly with increasing downstream distance [17]. For simple geometries, researchers have shown [17, 19, 20] that flame brush thickness scales well with arguments based on the turbulent diffusion of a passive scalar.

Lipatnikov and Chomiak [11] have noted that modeling the effect of the flame on the turbulence is much more difficult than modeling the effect of turbulence on the flame as there are a large number of unclosed terms in the

former problem [11]. The large number of unclosed terms further demonstrates the difficulty in making broad generalizations about the effect of the flame on the turbulence; there are a number of competing factors that can make the flame change the turbulent field that depend on the local flow conditions. Broadly speaking, the flame can generate turbulence through baroclinic torque effects (misaligned pressure and density gradients), produce or dissipate turbulence through combustion generated shear, and dissipate turbulence through dilatation [11]. As a result, whether or not a flame generates or dissipates turbulence is highly dependent on the local flow conditions [11, 12]. Additionally, Miles and Gouldin found the flame can cause anisotropic redistribution of turbulence where axial velocity fluctuations measured just across the flamelet are increased the most (or decreased the least) [12].

Non-reacting flow studies have shown that turbulence facilitates the production of scalar gradients as it tends to separate the scalar isosurfaces in the flow, which drives scalar dissipation [13, 21, 22]. Scalar dissipation in premixed flames is an important consideration for developing reaction rate models [11]. Reacting flow studies have shown that turbulence-flame interactions cause the preferential alignment of the flame-front normal perpendicular to the most extensive principal strain direction in close proximity of the flame [13, 14]. This perpendicular orientation of the most extensive principal strain rate with respect to the flame-front normal accounts for the production of scalar gradients.

Attempting to generalize these reacting flow features for single bluff body flames to multiple interacting bluff body flames is challenging due to a limited number of studies that have investigated interacting bluff-body flow fields [23-26]. However, some parallels can be drawn between bluff body flow fields and the features present in non-reacting interacting wakes and interacting plane jets, which have been the focus of numerous studies. These studies have shown that jet interaction can lead to a significant change in the jet structure, jet turbulence development, and jet instability characteristics [27-30]. Interacting jets fall into two categories: *unventilated jets*, where a surface is placed between the jet exits, and *ventilated jets*, where there is no surface between jets and air is free to flow between the two nozzles; here, we draw parallels between interacting unventilated plane jets and interacting bluff-body flows as the surface between the jets acts like a bluff body. Interacting plane jets are typically divided into three regions: the *converging region*, present in unventilated jets where the core flows and shear layers are separated by a recirculation zone, the *merging region*, where the shear layers begin to interact, and the *combined region*, where the two jets fully merge into a single jet. Interacting plane jets show significantly different characteristics from the initial development of a single jet in terms of the time-average flow trajectory and turbulence levels. This also implies that the development of the shear layers on either side of the jet, termed the “inner” and “outer” shear layers, can be influenced by the interaction.

Reported data about the turbulence levels in the converging and merging regions of the flow indicate that the profiles in these regions are non-self-similar and can differ significantly from single jets. The turbulence levels in the inner and outer shear layers grow at different rates as a function of downstream distance [29, 31, 32]. The turbulent stress profiles in these results show the uneven development of the inner and outer shear layers. At the jet exit, the turbulent stresses in the inner and outer shear layers were relatively similar, but mixing with the recirculation zone between the jets (or in the present work, the recirculation zone behind the bluff body) in the inner shear layer results in higher turbulent stresses, while entrainment of exterior fluid spreads the outer shear layer at a faster rate. Further results from Lin and Sheu [27] in a similar unventilated configuration indicated that the lateral turbulent stress is significantly greater in the merging region than in a single jet, as is the Reynolds stress. The enhanced Reynolds stress indicates that the transport of turbulent fluctuations laterally across the jet is enhanced beginning in the merging region. This may help explain the impact that fluctuations in the inner shear layer can have on the outer shear layer development, or the enhanced turbulence levels in the combined region. None of these turbulent profiles were self-similar in the converging or merging regions. Yuu *et al* [30] also examined the turbulence development of an interacting plane jet in both the converging and merging region of an interacting parallel plane jet and found the RMS of the velocity fluctuations to be anisotropic with higher fluctuations in the streamwise direction than the transverse direction. The turbulence anisotropy has been noted in other studies as well [27] and is important flow behavior in both non-reacting and reacting cases.

A small number of experimental studies have studied flame interaction in two-dimensional V-flames, primarily for the purposes of understanding the impact of flame interaction on thermoacoustic combustion instability [23-25, 33]. Francois *et al* [34] studied interacting, laminar, lean hydrogen-air V-flames stabilized by thin wires in order to understand the effect of non-unity Lewis numbers. They found that the jet profiles from the flames never fully merged due to the transverse velocities generated by the flame. This behavior is different than the behavior observed in non-reacting plane jets. However, more recent studies have focused on flame interaction in annular and can-annular gas turbine combustors [1, 2]. In these configurations, three-dimensional effects are important and the flames are typically swirl-stabilized, introducing a very complex flow field, which is beyond the scope of this work. As a result, we focus primarily on the work by Worth and Dawson, who studied two interacting axisymmetric bluff-body stabilized turbulent premixed flames [3, 35, 36]. Using OH-PLIF measurements, they reported that decreasing the spacing between the burners shifted the jet/flame merging location upstream, resulting in increased frequency of flame

merging and annihilation events due to the increased local turbulence intensity. In addition, as the flame separation distance was decreased the mean curvature was observed to become increasingly negative, which was also observed by Dunstan *et al.* [37, 38]. This shift is a result of the increased frequency of local flame interaction events that enhance cusping, which have negative flame curvatures. Finally, chemiluminescence and OH-PLIF measurements revealed enhancements in the turbulent flame brush thickness and chemiluminescence signal in the flame interaction region, which is consistent with the augmentation in flame surface density (FSD) observed in the OH-PLIF measurements. Extending these measurements to include acoustic forcing resulted in smaller coherent heat release rate fluctuations in cases with more flame interaction because of the more frequent flame interactions. Additionally, the flame surface density fluctuations increased at a greater rate than heat release rate fluctuations because of higher levels of mean flame stretch. The enhanced flame interaction increased nonlinearity in the flame response to input fluctuations because of frequent flame annihilation and sudden flame area fluctuations, as noted in Chen *et al.* [39]. A key point from these works is that the cumulative effects of multiple flames cannot be treated as a linear superposition of the effects of individual flames; rather, the non-linear interactions must be taken into account.

The focus of this work is to better understand how flame interaction affects key time-averaged features such as the mean velocity field, turbulence statistics, flame brush thickness, and flame surface density. In particular, we compare the time-averaged flow field and global flame characteristics of a single bluff-body stabilized flame to the center flame in an interacting flame configuration. We select the interacting flame configuration in which the center flame is most similar to the single flame configuration based on time-averaged velocity characteristics to compare flame brush thicknesses, turbulence trends, and flame surface density measurements.

## II. Experimental Overview

### A. Experimental Setup

All measurements are obtained in a 12 inch by 4 inch rectangular combustor using triangular prismatic bluff-bodies; a schematic of the test facility is shown in Figure 2 (a). The combustor burns a premixed mixture of air and natural gas. Two, 4 inch thick, 1/8 inch cell diameter plastic honeycombs are used to ensure uniform flow at the exit of the experiment. A metal perforated plate located 6 inches below the exit of the experiment acts as a flame arrestor to protect the honeycomb and improve the exit flow uniformity. Depending on the test configuration, one or three 0.75 inch wide triangular prismatic bluff-bodies are used for flame stabilization. The triangular bluff-body shape ensures that the flow field and flame structure are highly two-dimensional, thus enabling the use of planar diagnostics to capture flame and flow dynamics. Using one or three bluff bodies means the center flame, which is the flame of interest, is always subject to symmetric boundary conditions: either quiescent air or another flame. In the multiple-flame case, each bluff-body can be independently moved to achieve varying degrees of flame interaction. Two area reduction plates are used to change the open area of the experiment based on bluff body spacing. The open area is adjusted to ensure the spacing between the edge of the bluff body and the edge of the experiment is the same as the spacing between bluff bodies which prevents the jets from bending outward due to overexpansion at the exit. A line-of-sight CH\* chemiluminescence image obtained by averaging 8000 frames is shown in Figure 2 (b).

Two flame configurations are investigated in the paper: a single flame case and an interacting flame case. Each configuration is tested with inlet Reynolds numbers, based on bluff-body diameter, of 4000 and 6000 at an equivalence ratio of  $\phi = 0.8$ . The bluff body spacing for the interacting flame case is 52 mm between bluff body centers or 2.73 bluff body diameters ( $D$ ). This spacing was chosen because it has the most similar axial velocity field to the single flame.

### B. Diagnostics

A time-resolved, planar particle image velocimetry (PIV) measurement technique is used to collect two dimensional velocity data. The laser plane is located along the center plane of the experiment and captures velocities in the axial and cross-stream directions. The system consists of a high speed camera (Photron Fastcam SA 5 fitted with a Makro-Planar 100 mm lens), a high speed laser (Quantronix Hawk-Duo 532 nm Nd:YAG dual cavity laser), a particle seeder, and a PIV capture and analysis computer. A 532 nm band pass filter is used on the camera to remove flame luminescence. The flow is seeded with 0.5-2  $\mu\text{m}$  aluminum oxide particles. This results in a flamelet Stokes number of 0.0032 as defined by [40] and indicates the flow statistics are well captured in both the non-reacting and reacting regions of the flow. The PIV calculations are performed using DaVis 8.2.0 from LaVision. At each condition, 8001 images were obtained using a data acquisition rate of 4 kHz. The images were preprocessed using a sliding “subtract minimum” filter 5 frames long then processed into 8000 velocity fields with data rate of 2 kHz (half the

acquisition rate). Each velocity field consists of a minimum of 11,000 vectors, at least 100 in the downstream and at least 110 in the cross-stream directions, with a spatial resolution of 1.3 mm (about  $0.07D$ ). The vectors were calculated using a three-point Gaussian fit and a three-pass calculation; the first pass at an interrogation window size of  $64 \times 64$  and the second two passes with a size of  $16 \times 16$  and 50% overlap.

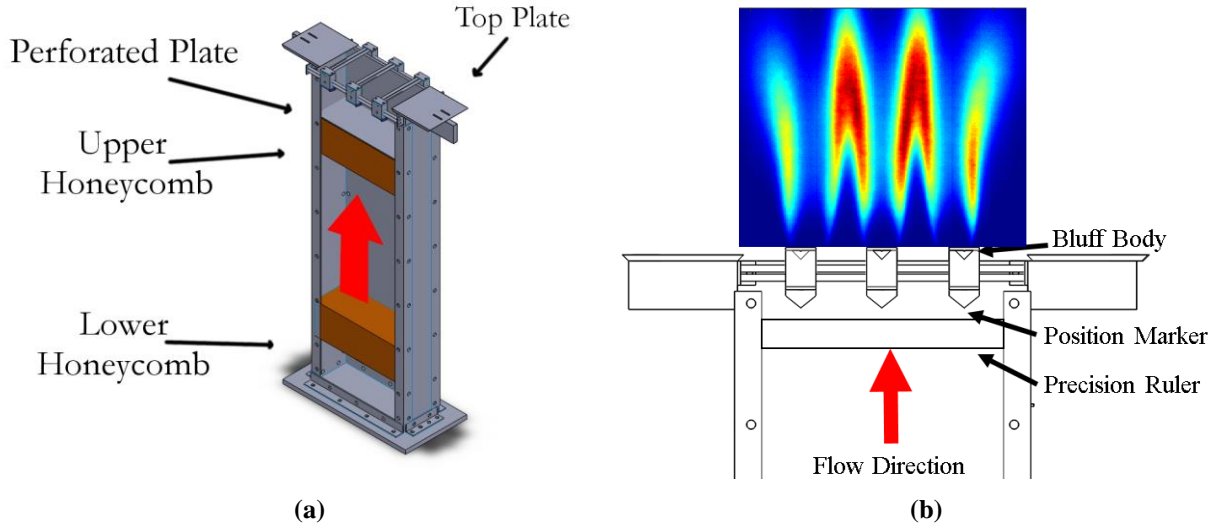


**Figure 2.** (a) Schematic of experimental setup (red arrow shows flow direction) and, (b) illustration of bluff-bodies with time-averaged chemiluminescence image.

During post-processing, vectors are rejected using the DaVis universal outlier detection scheme with a 3x median filter. The universal outlier detector scheme removes groups that have less than 5 vectors, vectors with a residual greater than 2, and reinserts vectors whose residual was less than 3. Finally, the rejected vectors are replaced with interpolated values. The average number of vectors replaced per dataset ranged from 5% to less than 7%. The percent first choice vectors are between 88% and 93% for the datasets analyzed in this paper. The velocity fields obtained from DaVis are used to obtain time-averaged contour plots, velocity profiles, and turbulence intensities at all locations in the flow field. Time-averaged statistics are computed by using all 8000 frames except in the  $2.73D$ ,  $Re=6000$  case where data collection issues limited this to 4000 frames. In addition to the PIV diagnostics, the bulk volume flow rates of the air and fuel are measured with Thermal Instrument Model 600-9/9500P digital flow meters. Two thermocouples are used to monitor the exhaust temperatures of the experiment.

### C. Dynamic Flame Binarization

The time-averaged progress variable  $\bar{c}$  is calculated by binarizing the filtered PIV images using a dynamic thresholding algorithm that reduces the sensitivity of the edge-detection to frame to frame intensity changes. The first step in this process is a median filter that is used to remove speckle noise followed by a bilateral filter, which is a noise reducing edge preserving filter as described in [41]. The bilateral filter helps to smooth out the specularity of the seeding particles in the non-reacting and reacting regions without blurring the edge between the regions. The final step is a thresholding then subsequent binarization of the filtered image based on Otsu's method [42]. Nonphysical holes in the reactants regions of the binarized image were algorithmically filled using morphological processing from the MATLAB image processing toolbox. This technique of finding flame positions by binarizing Mie-scattering PIV images is often referred to as conditioned particle image velocimetry (CPIV).

### D. Turbulence Statistics

The RMS of the velocity fluctuations and the Reynolds stresses were calculated using PIV data from the reacting cases. Other researchers [12, 15] have demonstrated the importance of using statistics conditioned on reactants or products to avoid issues with the burned/unburned intermittency. All reacting turbulence statistics have been reactant or product conditioned to reduce the effect of the burned/unburned intermittency on the statistics.

### III. Results

#### A. Rationale for single- to multi-flame comparison cases

To facilitate a direct comparison between interacting- and single-flame behaviors, we have chosen an interacting flame case with a very similar time-averaged flow field as the single-flame configuration. The time-averaged velocity field similarity is determined by comparing axial velocity profiles of single-flame cases to interacting flame cases at the same Reynolds number. The similarity of the profiles are quantified using Pearson correlation coefficients on the velocity profile calculated between  $y/D=-1$  and  $y/D=1$ . A correlation of 1 indicates an identical profile, while a correlation of -1 indicates perfectly opposite profile.

The single-flame case is compared with three multi-flame cases with different bluff-body spacings, and the results of the axial velocity profile comparisons are given in Table 1. Here, the velocity profile is compared at three downstream distances ( $x/D=1, 3,$  and  $5$ ). Figure 3 shows a representative plot of these comparisons. Note that in all plots in this paper  $y/D=0$  marks the center of the center bluff body and  $x/D=0$  is just downstream of the top of the bluff bodies. Figure 3 shows the multiple-flame case with a bluff body spacing of  $2.73D$  velocity profile compared to the single-flame configuration.

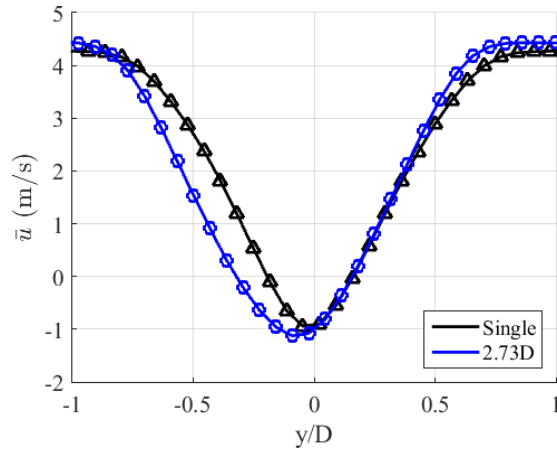


**Figure 3: Similarity of the velocity profiles of an interacting flame cases with a single flame case for  $Re=4000$  at  $x/D=2$ .**

In most cases, the time-averaged velocity profile correlation coefficient between the single-flame and multi-flame profiles decreases with downstream distance at a given Reynolds number. This indicates that for a given Reynolds number, the velocity profile near the exit of the experiment is governed more by bluff body geometry than the effect of interacting jets. These correlation coefficients indicate the  $2.73D$  spacing is most similar to the single flame configuration at both Reynolds numbers. For the rest of this work, the  $2.73D$  spacing is referred to as the interacting-flame case. Table 2 summarizes the inlet conditions for the conditions compared in more detail. Inlet turbulence levels are spatially averaged over the inlet region and taken from the reacting data at  $x/D=0.5$  to minimize the effect of laser reflections from the bluff bodies. The measurement uncertainty in bulk flow velocity and equivalence ratio  $\pm 0.08$  m/s and  $\pm 0.03$ , respectively; both these quantities are based on quoted uncertainty of the fuel and air flow meters. The 95% confidence interval on the inlet turbulence is shown in the table.

**Table 1: Summary of correlation coefficients for velocity profiles**

Axial Velocity Profile Correlation								
$Re=4000$	1.68D (32 mm)	2.20D (42 mm)	2.73D (52 mm)		$Re=6000$	1.68D (32 mm)	2.20D (42 mm)	2.73D (52 mm)
$x/D=1$	0.9664	0.9817	0.9505		$x/D=1$	0.9689	0.9886	0.9876
$x/D=3$	0.6841	0.9823	0.9405		$x/D=3$	0.9642	0.9587	0.9846
$x/D=5$	-0.2326	0.2988	0.7292		$x/D=5$	0.7313	0.8856	0.9793
<b>Average:</b>	0.4726	0.7543	0.8734		<b>Average:</b>	0.8881	0.9443	0.9838

**Table 2: Summary of inlet conditions for single flame versus interacting flame comparison**

Bluff-Body Spacing	Bulk Flow Velocity	Equivalence Ratio	Inlet Turbulence Level (%)	Bluff-Body Reynolds Number
Single	3.37	0.81	3.8±0.06	4000
Single	5.11	0.81	3.3±0.05	6000
Interacting	3.38	0.79	3.9±0.06	4000
Interacting	5.05	0.78	3.7±0.08	6000

**B. Flow Field Comparison**

Figure 4 shows the time-averaged axial velocity profiles for both the multiple-flame and single-flame configurations at  $x/D=1$ ,  $x/D=3$ , and  $x/D=5$  in black, blue, and red lines, respectively. Single flame velocity profiles are marked by triangles, while interacting flame cases are marked using squares. At  $x/D=1$ , the time-averaged reverse flow velocity in the interacting-flame case is lower, indicating a weaker recirculation zone behind the bluff body. This finding has interesting implications for flame anchoring, which depends on both thermal and fluid dynamic considerations. While prior work on interacting flames has shown that flame interaction increases local heat release rates [2] (which is beneficial to thermally anchoring flames), the trends from Figure 4 suggest that flame interaction in this configuration may be detrimental to flame anchoring fluid mechanically due to the reduction in backflow.

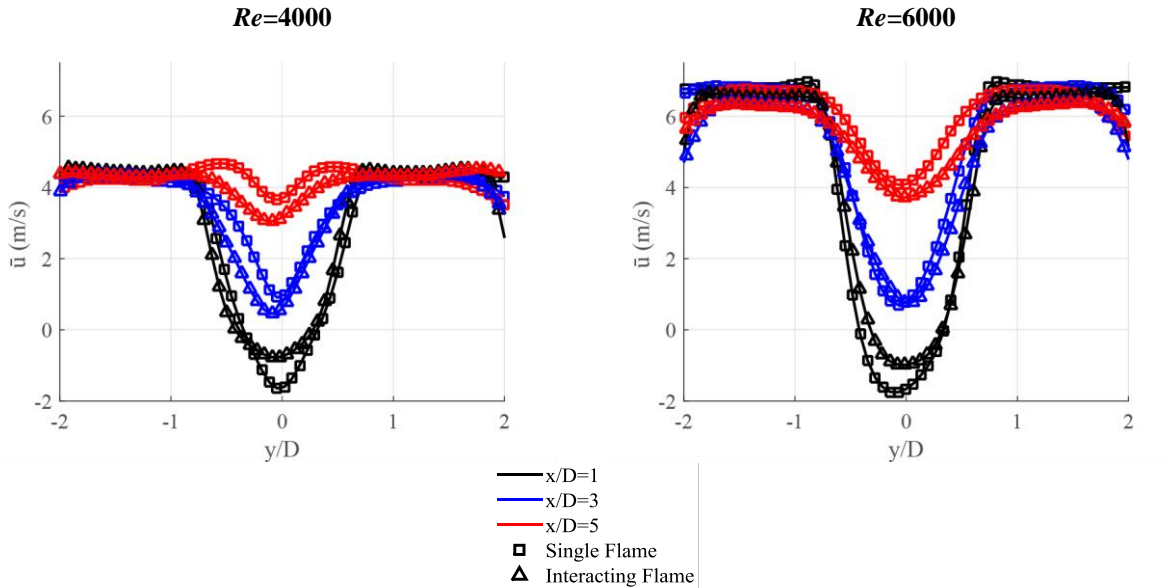


**Figure 4: Comparison of mean velocity profiles for various downstream locations between the single flame and interacting flame cases.**

### C. Flame Brush Comparison

Here, we use the time-averaged progress variable and the flame brush thickness as metrics to quantify the differences in flame behavior between the single-flame and multiple-flame cases. The value of the time-averaged progress variable,  $\bar{c}$ , ranges from 0 in regions that are always reactants to 1 in regions that are always products. The mean progress variable based on density can be defined as [43, 44]:

$$\bar{c} = \frac{\bar{\rho} - \rho_u}{\rho_b - \rho_u} \quad (1)$$

For consistency, the  $\bar{c} = 0.5$  contour is often used as a metric for the mean flame location, as suggested by Driscoll [17]. Since the progress variable represents a cumulative density function, the  $\bar{c} = 0.5$  contour is the median flame position, as noted by Shin and Lieuwen [45]. For the V-flame configuration in this experiment, the  $\bar{c} = 0.5$  contour and the time-averaged flame position are nearly identical; therefore, the  $\bar{c} = 0.5$  contour serves as an appropriate time-averaged flame location metric. A comparison of the location of the  $\bar{c} = 0.5$  contours is shown in Figure 5 below. This figure highlights the similarity in time-averaged flame location between the single and interacting flame cases at a given Reynolds number. The correlation coefficients between single and interacting flames are 0.9868 at  $Re=4000$  and 0.9611 at  $Re=6000$ .

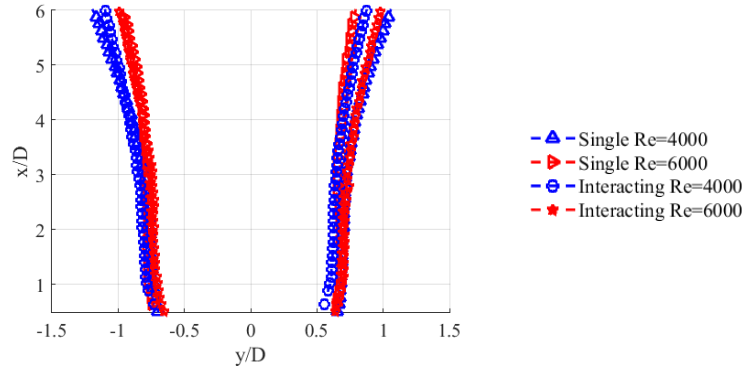


**Figure 5: Location of  $\bar{c} = 0.5$  contours for single and interacting flame cases.**

As mentioned earlier, the flame brush thickness represents the spatial region over which the instantaneous turbulent flame fronts are located [17]. The flame brush thickness can be related to the spatial distribution of heat release, which has important implications for combustion instabilities, emissions, and combustor liner thermal loadings. The flame brush thickness has been quantified using various methods. For instance, Gouldin and Miles quantified the flame brush thickness as the distance between the  $\bar{c} = 0.1$  and  $\bar{c} = 0.9$  in the direction normal to the  $\bar{c} = 0.5$  surface [16, 20]. Kheirkhah and Gülder [46], working from a formulation proposed by Namazian [44], have shown that flame brush thickness can be quantified using Equation (2). This formulation is based on the assumption that the turbulent flame can be instantaneously modeled as wrinkled laminar flame and that axial slices across the progress variable take the form of a complementary error function [46]. Using these assumptions, we can determine the flame brush thickness using Equation (2). Lipatnikov and Chomiak [19] showed that despite the various definitions of the flame brush thickness, if the distance through the flame brush is normalized by the flame brush thickness and plotted as a function of the progress variable contour, the data is collapsed on to a complementary error function profile. Therefore, we expect the trends reported in this paper to hold for other definitions of flame brush thickness.

$$\delta_t = \frac{1}{\max \left| \frac{\partial \bar{c}}{\partial y} \right|} \quad (2)$$

Plots of flame brush thickness versus non-dimensionalized downstream distance for both Reynolds numbers and flame configurations are shown in Figure 6. The plots show every fourth point for clarity and the blue and red symbols correspond to Reynolds numbers of 4000 and 6000, respectively. The results for the left flame branch are shown on the left while the results for the right flame branch are shown on the right. For a given flame configuration, the flame brush growth is faster at higher Reynolds numbers, as has been noted by Tamadonfar and Gülder [18]. The more

interesting implication of Figure 6 is that for both Reynolds numbers, the flame brush in the multiple-flame configuration grows faster with downstream distance than that of the single-flame configuration. This finding indicates that flame interaction enhances flame brush growth in this configuration. Due to the similarity in the left and right flame branches, only data from the left branch is shown in the rest of the paper. The reason for the increased flame brush growth in the interacting case is increased flame wrinkling which will be explained in the next section.

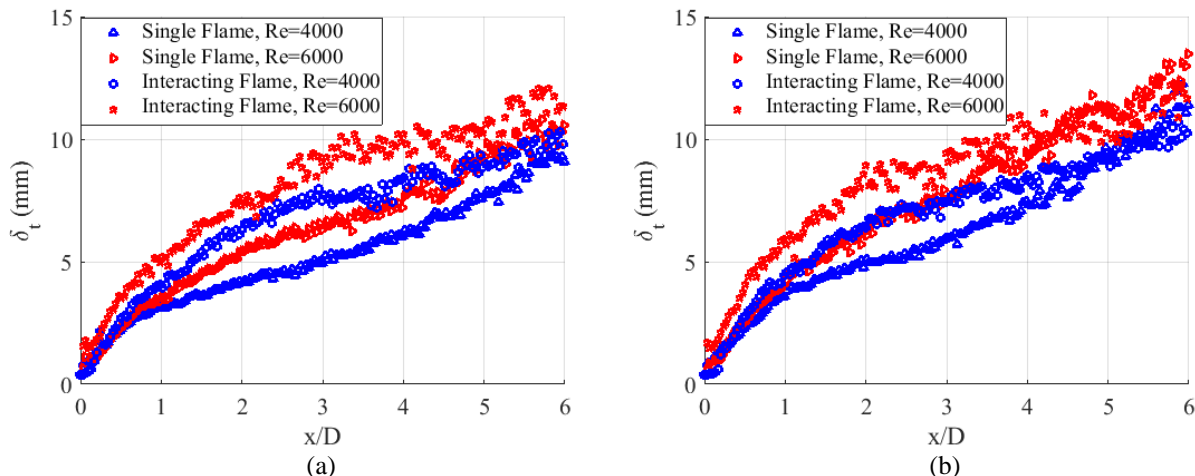


**Figure 6: Comparison of flame brush thickness versus  $x/D$  for (a) left flame branch and (b) right flame branch.**

#### D. Flame Surface Density Comparison

Flame surface density (FSD) is defined as the ratio of local area to volume of a flame for a given differential volume [47, 48]. Broadly speaking, it is a measure of flame wrinkling, and studies have shown that FSD is an important parameter in the estimation of local characteristics of flames, including local consumption speed and heat release rate [47]. Measurement of the three-dimensional FSD can be obtained through simulations, however, we report two-dimensional FSD that has been measured with high-speed planar diagnostics\*. The two-dimensional FSD was calculated by drawing a 10 mm diameter circle at every spatial location along the flame edge and recording the length of the flame within that circle. The ratio of this length to the area of the circle provided the local FSD value. Averaging of this local FSD value at specific downstream locations was done over the total number of frames to provide a time averaged FSD ( $\bar{\Sigma}$ ), as formulated in Equation 3.

$$\bar{\Sigma} = \frac{1}{N} \sum \left( \frac{L}{A} \right) \quad (3)$$

Figure 7 shows  $\bar{\Sigma}$  in progress variable space at different downstream locations for the single and interacting flames at two different Reynolds numbers. A bin size of 0.01 was used in the progress variable space for  $\bar{\Sigma}$ . The trends in this figure suggest that an increase in Reynolds number does not significantly change  $\bar{\Sigma}$  for both single and interacting flames. Previous results show that the FSD progressively decreases as a function of downstream distance, which is reflected here for both the single-flame and interacting-flame cases [47, 48]. The decrease in FSD may be a result in the increase in the frequency of flame interaction events, a known mechanism of flame-area destruction [37, 38]. As seen in Figure 7, the decay of  $\bar{\Sigma}$  with downstream distance is faster in the interacting flame as compared to the single flame. The increased flame brush thickness in the interacting flame configurations causes the flame surface density to take on more values in the progress variable space, resulting in lower  $\bar{\Sigma}$  values for the interacting flames in a given bin as compared to the single flames. This is observed for both Reynolds numbers and is likely the result of the interaction events.

\* This was done by cropping the edges obtained from the edge-detection algorithm to a 98.12 mm high window (about  $x/D=0.36 - x/D=5.511$ ). Mapping of progress variable was done to record the nearest progress variable value at each spatial location on the edge for all the frames.

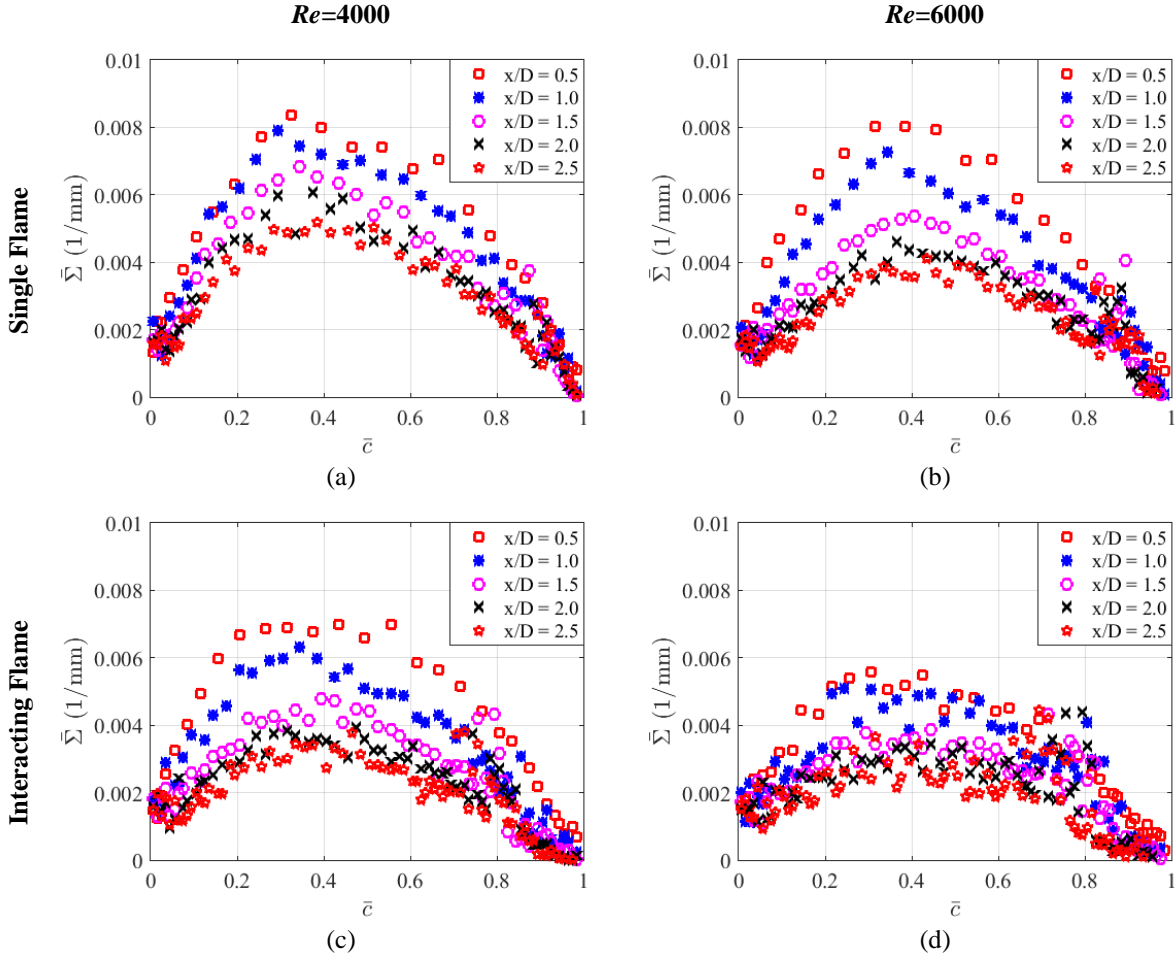


**Figure 7:**  $\bar{\Sigma}$  at various downstream locations for the single and interacting flame case at a Reynolds number of (a) and (c)  $Re=4000$ , and (b) and (d)  $Re=6000$ .

Figure 8 shows  $\bar{\Sigma}$  as a function of downstream distance. This figure shows that at a given Reynolds number, the flame surface density is higher for the interacting flame than the single flame case until about three bluff body diameters downstream, where they become very similar. This trend indicates that the flame wrinkles are created at the base of the flame and decay as they are convected downstream. These trends in FSD can also help to explain the differences in flame brush growth between single and interacting flames. Flame brush growth is driven by flame wrinkling. The increase in FSD at the base of the flame for interacting flame configurations indicates more flame wrinkling, where more wrinkling means a thicker flame brush for interacting configurations. Additionally, Figure 8 shows that the differences in flame wrinkling between the single and interacting flame configurations are largest between 0.5 and 3 diameters downstream, despite the fact that the time-averaged flame intersection points for the interacting flame cases are much farther downstream ( $x/D=8$  for  $Re=4000$ ,  $x/D=8.8$  for  $Re=6000$ ). This result indicates that the effects of flow and flame interaction are felt throughout the flow field and are not limited to the flame intersection point. As such, flow fields with flame interaction cannot be divided into regions where flame interaction is ignored and regions where it is not – the entire flow field and flame development are affected by the interaction phenomenon. The mechanism which drives the increased flame wrinkling in the interacting flame case may be explained by examining the reactant turbulence statistics.

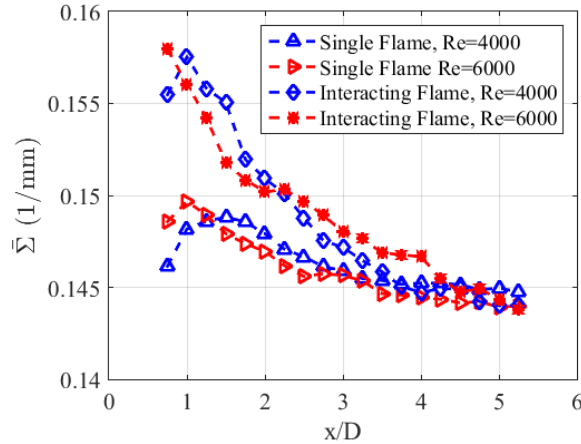


Figure 8:  $\bar{\Sigma}$  as a function of downstream distance along the  $\bar{c} = 0.5$  for single flame and interacting flame cases.

### E. Reactant Conditioned Turbulence Along $\bar{c}=0.5$ Isocontour

Behavior of the flame sheet is controlled by turbulence in the reactants [11]. In an effort to understand the reason for the increased flame wrinkling in the interacting flame case, the reactant-conditioned turbulence statistics along the  $\bar{c} = 0.5$  isocontour are compared between the single-flame and multiple-flame case in Figure 9\*. For clarity, every twelfth data point is shown. Figure 9 indicates that the total turbulence intensity is essentially the same between the interacting flame and single flame cases. However, since shear flows have anisotropic turbulence, this result may be better understood by examining the streamwise ( $u_{11}$ ) and cross-stream ( $u_{22}$ ) Reynolds stresses. These components are shown in Figure 10. For clarity, every twelfth data point is shown. For both Reynolds numbers, the  $u_{22}$  component is higher in the interacting flame case than it is for the single flame case. In contrast, the  $u_{11}$  component is essentially the same between flame configurations but multiple times greater than the  $u_{22}$  component. As a result, the overall turbulence intensity is dominated by the  $u_{11}$  component. Reynolds stress trends similar to these have been reported in the non-reacting interacting plane jet literature [27, 30].

The flame sheet normals are nominally perpendicular to the direction of flow, so the  $u_{22}$  stresses fluctuate parallel to the flame normal direction. The increased cross-stream Reynolds stresses in the interacting flame case appears to be the reason for the increased flame wrinkling in the interacting flame case. Tamadonfar and Gülder [18] also reported an increase in flame brush thickness with increasing turbulence intensity for axisymmetric turbulent Bunsen flames. While a slice through an axisymmetric Bunsen flame seems to resemble two interacting V-flames, the turbulence field is more isotropic in an axisymmetric turbulent Bunsen flame than in this turbulent V-flame. This result indicates the anisotropy of the turbulence is what drives the changes in flame wrinkling, which in turn drives the changes in flame brush growth. Another important trend to notice in Figure 10 is that the differences in Reynolds stresses are most prominent between 0.5 and 4 diameters downstream. These differences in trends are again well upstream of the time-averaged intersection point, which highlights how flame and flow interaction impacts the whole flow field. These trends also highlight the importance of the near bluff body region to downstream flow evolution. Finally, this region of increased cross-stream Reynolds stresses also aligns with the region of enhanced FSD, again showing the link between cross-stream Reynolds stress and turbulent flame wrinkling.

\* Since the coordinate of the  $\bar{c} = 0.5$  contour may not have a matching coordinate in the turbulence fields due to the lower resolution of the PIV data, cubic interpolation from the progress variable to the vector fields was used.

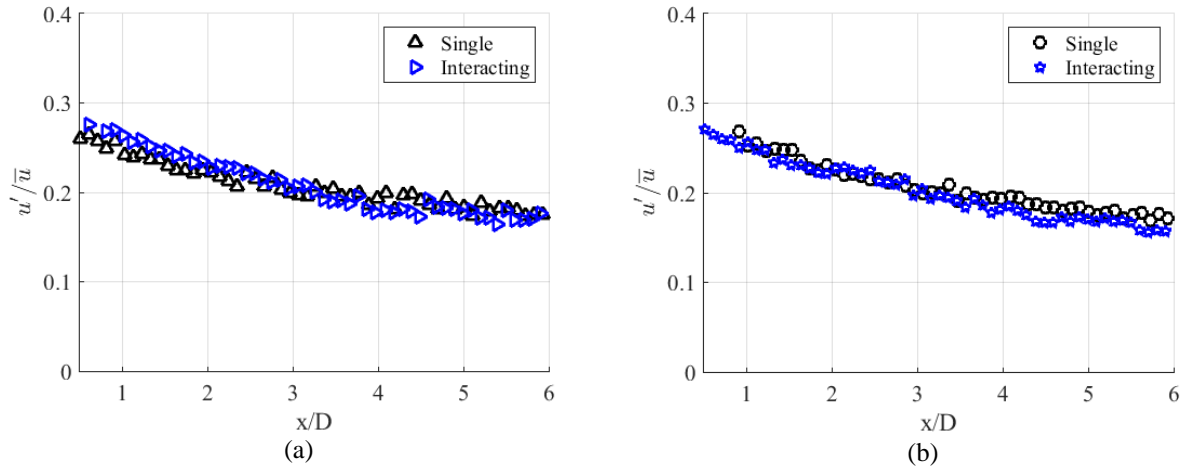


Figure 9: Reactant conditioned total turbulence intensity plotted along the  $\bar{c}=0.5$  contour for the interacting flame and single flame case for (a)  $Re=4000$  and (b)  $Re=6000$ .

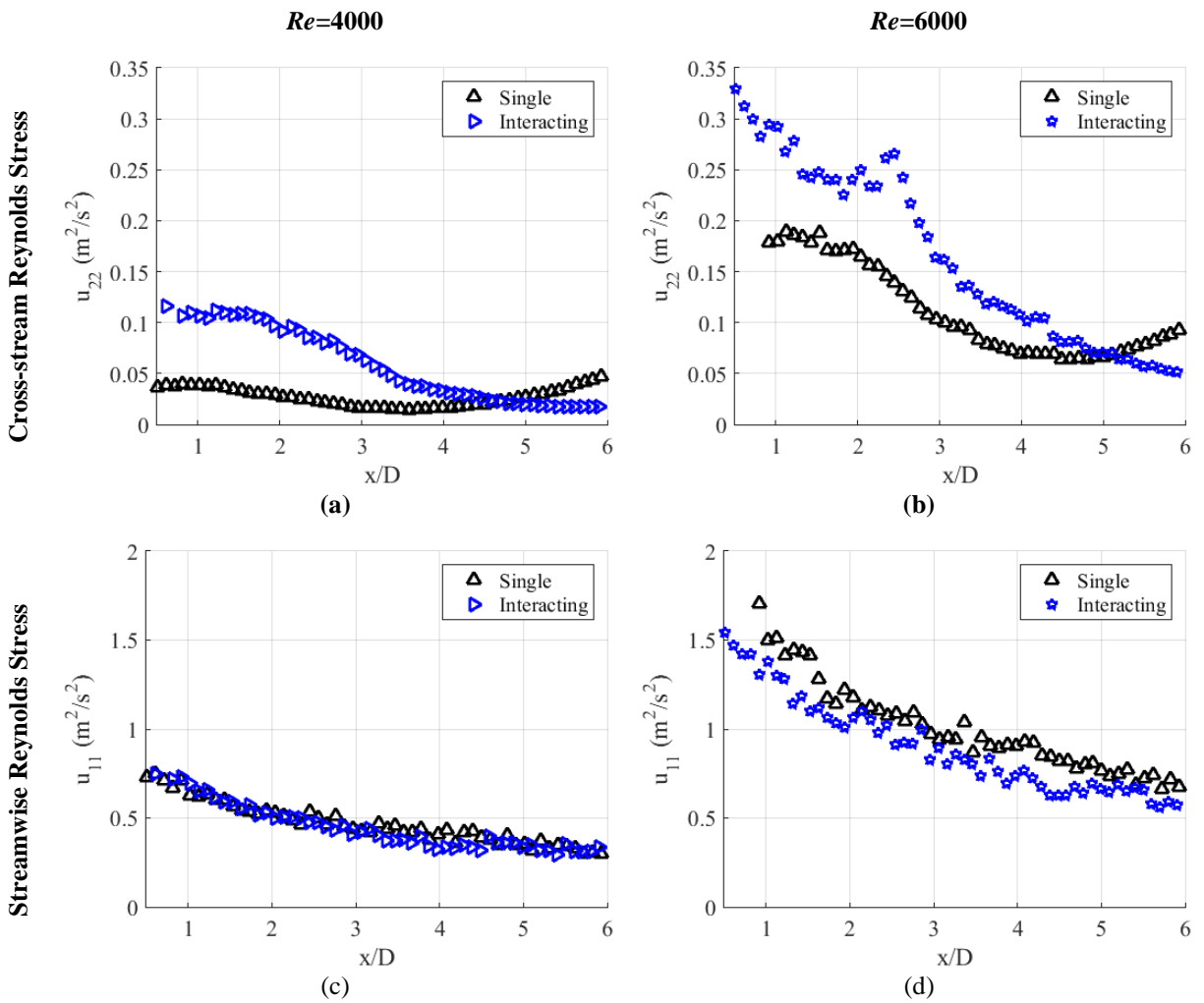


Figure 10: Reactant conditioned Reynolds stress components plotted along the  $\bar{c}=0.5$  contour for the interacting flame and single flame case at a Reynolds number of (a) and (c) 4000, and (b) and (d) 6000.

## F. Product Conditioned Turbulence Along $\bar{c}=0.5$ Isocontour

In the previous sections we focused on the effect of turbulence on the flame by examining reactant conditioned statistics. In this section we focus on the effect of the flame on the turbulence by examining product conditioned turbulence statistics. Figure 11 shows the product-conditioned Reynolds stress components along the  $\bar{c} = 0.5$  isocontour compared to the reactant conditioned Reynolds stresses for both flame configurations. The product conditioned statistics are in shades of red, while the reactant conditioned statistics are in blue and black. In all cases, the interacting flame has higher Reynolds stresses in the products than the single flame at a given Reynolds number. Additionally, the product conditioned  $u_{22}$  component is always higher than the reactant conditioned one for the interacting flame while the same is not true for the single flame. Also note that in general, the  $u_{11}$  component is less than the reactant conditioned one at a given downstream location. The trace of the Reynolds stress tensor is the turbulent kinetic energy, therefore, one can use the comparison of reactant and product Reynolds stress in Figure 11 as a way to measure the redistribution of turbulent kinetic energy. These trends suggest that both flame configurations tend to enhance the  $u_{22}$  component while reducing the  $u_{11}$  component, therefore redistributing the turbulence anisotropically. The increase of  $u_{22}$  in the products can be explained by looking at the orientation of the flame sheet as a function of downstream distance.

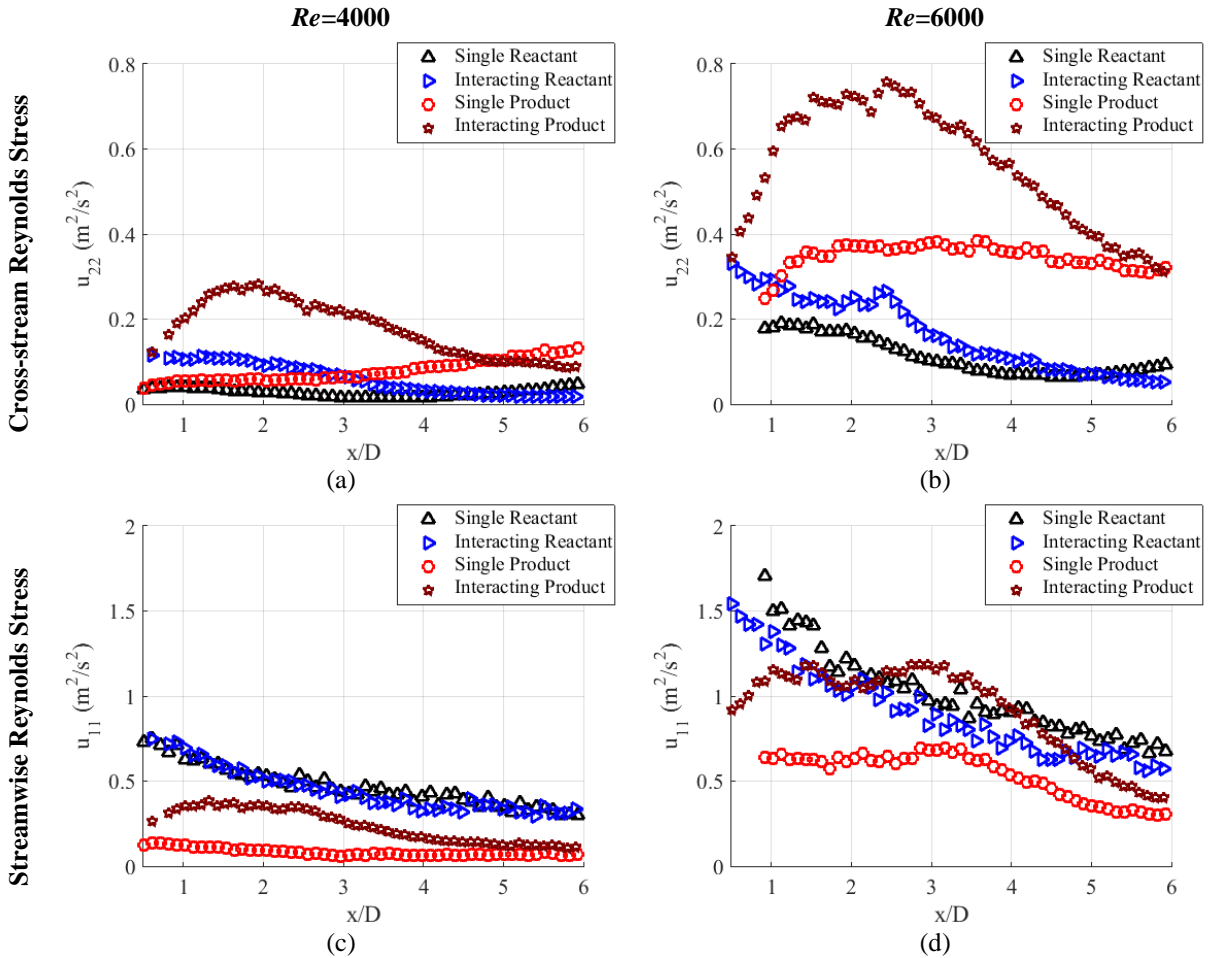
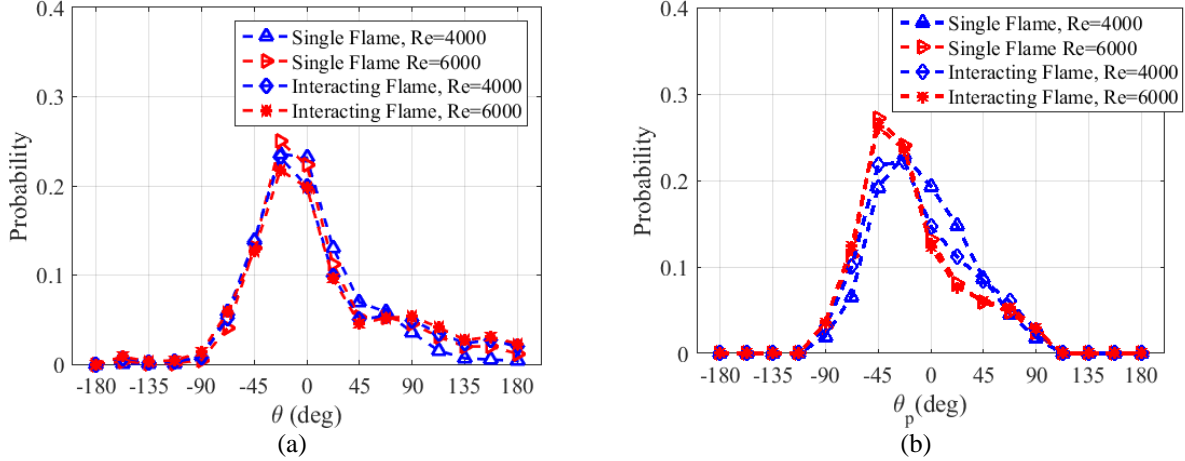


Figure 11: Comparison of reactant and product conditioned Reynolds stress components along the  $\bar{c} = 0.5$  isocontour for (a) and (c)  $Re=4000$  (b) and (d)  $Re=6000$ .

## G. Instantaneous Flame Normals

Although the flame sheet resembles the  $\bar{c} = 0.5$  isocontour plot in Figure 5 in a time-averaged sense, on an instantaneous basis, the flame is extremely wrinkled. Therefore, the flame surface normals point in a number of

different directions at any given time. Figure 12(a) shows a probability distribution plot of flame surface normal orientations ( $\theta$ ), which are measured with respect to the  $x_2$  direction towards the reactants. This figure indicates that in a time-averaged sense, a plurality (between 40% and 50%) of the normal vectors are oriented in the ranges of  $[-5^\circ, +5^\circ]$  and  $[-35^\circ, -25^\circ]$  towards the reactants. This finding indicates the preferred orientation of the flame normal is more perpendicular than parallel to the incoming flow. This also indicates that the gas expansion across the flame is primarily in the  $x_2$  direction in a time-averaged sense. This is likely why the  $u_{22}$  component of Reynolds stress is preferentially enhanced; the instantaneous flame normal directions redistribute turbulent fluctuations primarily in the  $x_2$  direction.



**Figure 12: Probability of (a) flame-front normal vector orientations from instantaneous flame edges, and (b) principal strain angles ( $\theta_p$ ) from the instantaneous strain rate tensors plotted along the  $\bar{c}=0.5$  contour for the interacting and single flame case for  $Re=4000$  and  $Re=6000$ .**

This behavior of the normal vectors can be related to the principal angles of the instantaneous strain rate tensor. The instantaneous strain rate tensor is given by (4), where  $U_i$  is the instantaneous velocity in the  $i$ -direction.

$$S_{ij} = \frac{1}{2} \left( \frac{\partial U_i}{\partial x_j} + \frac{\partial U_j}{\partial x_i} \right) \quad (4)$$

From the instantaneous strain rate tensor, the principal strain angle  $\theta_p$  is obtained as:

$$\theta_p = \frac{1}{2} \tan^{-1} \left( \frac{2S_{12}}{S_{11} - S_{22}} \right) \quad (5)$$

Figure 12(b) shows a probability distribution plot of principal angles calculated from the instantaneous strain rate tensors along the  $\bar{c} = 0.5$  isocontour. Principal strain angles along the  $\bar{c} = 0.5$  isocontour, obtained from equation (5), align with the most probable flame-front normal angles. This alignment of the principal strain angles with the flame-front normal angles follows up with the alignment of the most extensive principal strain being perpendicular to the flame-front normal in close proximity of the flame, suggesting the preference of the flame to align with the most compressive strains. This indicates that scalar gradients are being produced in the  $x_2$  direction, which supports the above findings about the enhancement of  $u_{22}$  component.

#### IV. Conclusions and Future Work

This work has compared the flame brush thickness of a single flame to an interacting flame. To facilitate a direct comparison between interacting and single-flame behaviors, we have chosen an interacting flame case with a very similar time-averaged flow field as the single-flame configuration. Flame interaction caused an increase in flame brush thickness due to an increase in flame wrinkling as indicated by FSD plots. The increased flame wrinkling observed in the interacting configurations is caused by increased  $u_{22}$  components of Reynolds stress. The increase in Reynolds stress is due to a complex flame/flow interaction. In the product gases, the  $u_{22}$  component of Reynolds stress is enhanced over the  $u_{11}$  component due to flame normals being preferentially oriented in the  $x_2$  direction. Furthermore, this enhancement of  $u_{22}$  is higher in the interacting flame case. The results of this study indicate that flame interaction is a nonlinear process that cannot be represented by the superposition of single flames.

The first implication of this work is that the effects of flame and flow interaction are felt throughout the flow and are not simply confined to the flame intersection point. The flows investigated in this work are all low Mach number flows so it is expected that downstream boundary conditions will have effects on the entire flow field. The turbulence fluctuations and FSD as a function of downstream distance suggest the differences in the interacting and single flame cases are driven by differences between the flame anchoring location and about 3 diameters downstream. These results further indicate flows with interacting flames cannot be subdivided into regions where flame interaction can be neglected and regions where it cannot. The turbulence statistics indicate that anisotropy is an important consideration in shear flows such as these. The  $u_{22}$  component of Reynolds stress, which is primarily parallel to the flame normal direction, is the driver of flame wrinkling behavior and flame brush thickness trends. Flame area changes contribute to global heat release changes which is important for flame dynamics and combustion instability. Flame wrinkling is an important contributor to flame area changes and the FSD results of this work indicate that interacting flames have more flame wrinkling. This suggests that interacting flames have more rapid heat release changes which has implications for combustion instability. Product conditioned turbulence statistics indicate that flames tend to redistribute turbulent kinetic energy anisotropically by enhancing fluctuations in the cross stream direction. The enhancement of cross-stream turbulence levels in the products is supported by instantaneous flame normal angle analysis indicating the most probably flame normal direction is between angles of  $[-5^\circ, +5^\circ]$  and  $[-35^\circ, -25^\circ]$  towards the reactants. Product conditioned turbulence statistics are important for pollution control and emissions applications.

Future work will extend this analysis to other interacting flame configurations with different spacings between bluff bodies. In particular, the analysis will focus on using turbulence statistics and FSD results as a way to understand the differences in flame brush growth between different interacting flame configurations. Comparisons will be made between reacting and non-reacting data in an effort to differentiate flame interaction effects from flow interaction effects.

## V. Acknowledgments

The authors would like to thank Mr. Larry Horner, Dr. Stephen Peluso, Dr. Bryan Quay, Michael Meehan and Janith Samarasinghe for their contributions to this work.

## VI. References

1. Samarasinghe, J., Peluso, S., Szedlmayer, M., De Rosa, A., Quay, B., and Santavicca, D. "Three-Dimensional Chemiluminescence Imaging of Unforced and Forced Swirl-Stabilized Flames in a Lean Premixed Multi-Nozzle Can Combustor," *Journal of Engineering for Gas Turbines and Power* Vol. 135, No. 10, 2013, p. 101503.
2. Samarasinghe, J., Peluso, S. J., Quay, B. D., and Santavicca, D. A. "The Three-Dimensional Structure of Swirl-Stabilized Flames in a Lean Premixed Multinozzle Can Combustor," *Journal of Engineering for Gas Turbines and Power* Vol. 138, No. 3, 2015, p. 031502.
3. Worth, N. A., and Dawson, J. R. "Cinematographic OH-PLIF measurements of two interacting turbulent premixed flames with and without acoustic forcing," *Combustion and Flame* Vol. 159, No. 3, 2012, pp. 1109-1126.
4. Shanbhogue, S. J., Husain, S., and Lieuwen, T. "Lean blowoff of bluff body stabilized flames: Scaling and dynamics," *Progress in Energy and Combustion Science* Vol. 35, No. 1, 2009, pp. 98-120.
5. Penner, S. S., and Williams, F. "Recent Studies on Flame Stabilization of Premixed Turbulent Gases," *Applied Mechanics Reviews* Vol. 10, No. 6, 1957, pp. 229-237.
6. Prasad, A., and Williamson, C. H. K. "The instability of the shear layer separating from a bluff body," *Journal of Fluid Mechanics* Vol. 333, 1997, pp. 375-402.
7. Erickson, R. R., and Soteriou, M. C. "The influence of reactant temperature on the dynamics of bluff body stabilized premixed flames," *Combustion and Flame* Vol. 158, No. 12, 2011, pp. 2441-2457.
8. Zhou, Y., and Antonia, R. A. "A study of turbulent vortices in the near wake of a cylinder," *Journal of Fluid Mechanics* Vol. 253, 1993, pp. 643-661.
9. Ong, L., and Wallace, J. "The velocity field of the turbulent very near wake of a circular cylinder," *Experiments in Fluids* Vol. 20, No. 6, 1996, pp. 441-453.
10. Braza, M., Perrin, R., and Hoarau, Y. "Turbulence properties in the cylinder wake at high Reynolds numbers," *Journal of Fluids and Structures* Vol. 22, No. 6-7, 2006, pp. 757-771.

11. Lipatnikov, A. N., and Chomiak, J. "Effects of premixed flames on turbulence and turbulent scalar transport," *Progress in Energy and Combustion Science* Vol. 36, No. 1, 2010, pp. 1-102.
12. Miles, P., and Gouldin, F. "Premixed turbulent flame/flow interaction: Simultaneous measurements of velocity and flamelet position," *AIAA Journal* Vol. 36, No. 7, 1998, pp. 1178-1189.
13. Sponfeldner, T., Boxx, I., Beyrau, F., Hardalupas, Y., Meier, W., and Taylor, A. M. K. P. "On the alignment of fluid-dynamic principal strain-rates with the 3D flamelet-normal in a premixed turbulent V-flame," *Proceedings of the Combustion Institute* Vol. 35, No. 2, 2015, pp. 1269-1276.
14. Steinberg, A. M., Driscoll, J. F., and Swaminathan, N. "Statistics and dynamics of turbulence-flame alignment in premixed combustion," *Combustion and Flame* Vol. 159, No. 8, 2012, pp. 2576-2588.
15. Pfadler, S., Leipertz, A., and Dinkelacker, F. "Systematic experiments on turbulent premixed Bunsen flames including turbulent flux measurements," *Combustion and Flame* Vol. 152, No. 4, 2008, pp. 616-631.
16. Gouldin, F. C., and Miles, P. C. "Chemical closure and burning rates in premixed turbulent flames," *Combustion and Flame* Vol. 100, No. 1-2, 1995, pp. 202-210.
17. Driscoll, J. F. "Turbulent premixed combustion: Flamelet structure and its effect on turbulent burning velocities," *Progress in Energy and Combustion Science* Vol. 34, No. 1, 2008, pp. 91-134.
18. Tamadonfar, P., and Gülder, Ö. L. "Flame brush characteristics and burning velocities of premixed turbulent methane/air Bunsen flames," *Combustion and Flame* Vol. 161, No. 12, 2014, pp. 3154-3165.
19. Lipatnikov, A. N., and Chomiak, J. "Turbulent flame speed and thickness: phenomenology, evaluation, and application in multi-dimensional simulations," *Progress in Energy and Combustion Science* Vol. 28, No. 1, 2002, pp. 1-74.
20. Venkateswaran, P. "Measurements and Modeling of Turbulent Consumption Speeds of Syngas Fuel Blends," *School of Aerospace Engineering*. Vol. Ph.D., Georgia Institute of Technology, Atlanta, Georgia, 2013.
21. Kerr, R. M. "Higher-order derivative correlations and the alignment of small-scale structures in isotropic numerical turbulence," *Journal of Fluid Mechanics* Vol. 153, 1985, pp. 31-58.
22. Buxton, O. R. H., and Ganapathisubramani, B. "Amplification of enstrophy in the far field of an axisymmetric turbulent jet," *Journal of Fluid Mechanics* Vol. 651, 2010, pp. 483-502.
23. Reuter, D., Hegde, U., and Zinn, B. "Flowfield measurements in an unstable ramjet burner," *Journal of Propulsion and Power* Vol. 6, No. 6, 1990, pp. 680-685.
24. Hegde, U., Reuter, D., Daniel, B., and Zinn, B. "Flame driving of longitudinal instabilities in dump type ramjet combustors," *Combustion Science and Technology* Vol. 55, No. 4-6, 1987, pp. 125-138.
25. Hegde, U., Reuter, D., and Zinn, B. "Sound generation by ducted flames," *AIAA Journal* Vol. 26, No. 5, 1988, pp. 532-537.
26. Williamson, C. H. K. "Evolution of a single wake behind a pair of bluff bodies," *Journal of Fluid Mechanics* Vol. 159, 1985, pp. 1-18.
27. Lin, Y., and Sheu, M. "Investigation of two plane parallel unventilated jets," *Experiments in Fluids* Vol. 10, No. 1, 1990, pp. 17-22.
28. Lin, Y., and Sheu, M. "Interaction of parallel turbulent plane jets," *AIAA Journal* Vol. 29, No. 9, 1991, pp. 1372-1373.
29. Nasr, A., and Lai, J. "Two parallel plane jets: mean flow and effects of acoustic excitation," *Experiments in Fluids* Vol. 22, No. 3, 1997, pp. 251-260.
30. Yuu, S., Shimoda, F., and Jotaki, T. "Hot wire measurement in the interacting two-plane parallel jets," *AIChE Journal* Vol. 25, No. 4, 1979, pp. 676-685.
31. Miller, D. R., and Comings, E. W. "Force-momentum fields in a dual-jet flow," *Journal of Fluid Mechanics* Vol. 7, No. 02, 1960, pp. 237-256.
32. Ko, N., and Lau, K. "Flow structures in initial region of two interacting parallel plane jets," *Experimental Thermal and Fluid Science* Vol. 2, No. 4, 1989, pp. 431-449.
33. Elias, I. "Acoustical Resonances Produced by Combustion of a Fuel-Air Mixture in a Rectangular Duct," *The Journal of the Acoustical Society of America* Vol. 31, No. 3, 1959, pp. 296-304.
34. Francois, I., Larrauri, D., and Escudié, D. "Interaction between two premixed laminar V-shaped flame fronts at low Lewis number," *Combustion and Flame* Vol. 110, No. 1-2, 1997, pp. 14-24.
35. Worth, N. A., and Dawson, J. R. "Tomographic reconstruction of OH\* chemiluminescence in two interacting turbulent flames," *Measurement Science and Technology* Vol. 24, No. 2, 2013, p. 024013.
36. Worth, N. A., and Dawson, J. R. "Modal dynamics of self-excited azimuthal instabilities in an annular combustion chamber," *Combustion and Flame* Vol. 160, No. 11, 2013, pp. 2476-2489.
37. Dunstan, T., Swaminathan, N., Bray, K., and Kingsbury, N. "Flame interactions in turbulent premixed twin V-flames," *Combustion Science and Technology* Vol. 185, No. 1, 2013, pp. 134-159.

38. Dunstan, T., Swaminathan, N., Bray, K., and Kingsbury, N. "The effects of non-unity Lewis numbers on turbulent premixed flame interactions in a twin V-flame configuration," *Combustion Science and Technology* Vol. 185, No. 6, 2013, pp. 874-897.
39. Chen, J. H., Echekki, T., and Kollmann, W. "The mechanism of two-dimensional pocket formation in lean premixed methane-air flames with implications to turbulent combustion," *Combustion and Flame* Vol. 116, No. 1-2, 1999, pp. 15-48.
40. Picano, F., Battista, F., Troiani, G., and Casciola, C. M. "Dynamics of PIV seeding particles in turbulent premixed flames," *Experiments in Fluids* Vol. 50, No. 1, 2011, pp. 75-88.
41. Paris, S., and Durand, F. "A Fast Approximation of the Bilateral Filter using a Signal Processing Approach." Massachusetts Institute of Technology, Cambridge, Massachusetts, 2006.
42. Gonzalez, R. C., and Woods, R. E. *Digital Image Processing*: Prentice Hall, 2002.
43. Kheirkhah, S., and Gülder, Ö. L. "Turbulent premixed combustion in V-shaped flames: Characteristics of flame front," *Physics of Fluids (1994-present)* Vol. 25, No. 5, 2013, p. 055107.
44. Namazian, M., Shepherd, I. G., and Talbot, L. "Characterization of the density fluctuations in turbulent V-shaped premixed flames," *Combustion and Flame* Vol. 64, No. 3, 1986, pp. 299-308.
45. Shin, D.-H., and Lieuwen, T. "Flame wrinkle destruction processes in harmonically forced, turbulent premixed flames," *Journal of Fluid Mechanics* Vol. 721, 2013, pp. 484-513.
46. Kheirkhah, S., and Gülder, Ö. L. "Topology and Brush Thickness of Turbulent Premixed V-shaped Flames," *Flow, Turbulence and Combustion* Vol. 93, No. 3, 2014, pp. 439-459.
47. Shepherd, I. G. "Flame surface density and burning rate in premixed turbulent flames," *Symposium (International) on Combustion* Vol. 26, No. 1, 1996, pp. 373-379.
48. Veynante, D., Duclos, J. M., and Piana, J. "Experimental analysis of flamelet models for premixed turbulent combustion," *Symposium (International) on Combustion* Vol. 25, No. 1, 1994, pp. 1249-1256.